Supplementary Material, Part 1

We present in the first section of this supplement two figures that support the main text and are referenced in the discussion the Williams Flats Fire (Sections 3.1 and 3.2). In addition, we provide a figure showing the locations of all transverse and longitudinal transects made by the DC-8. Lastly, we provide a table referenced in the main text that describes the particle climatology of the MISR RA (Section 2.1).
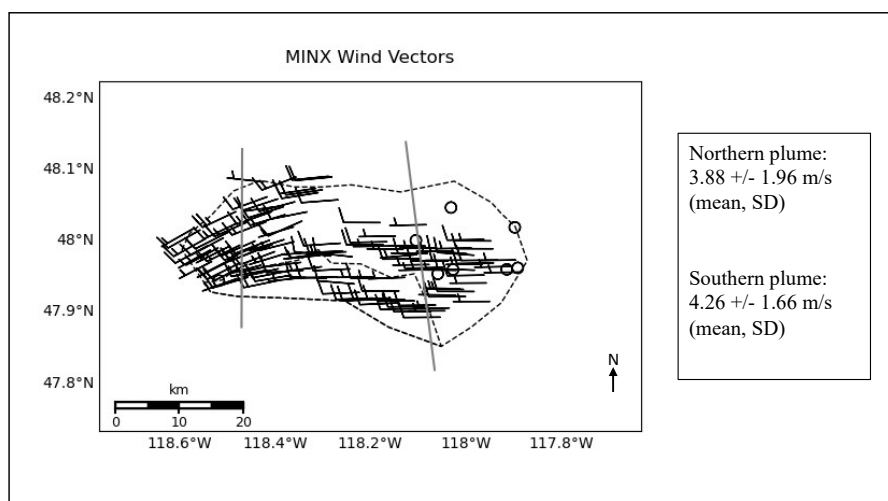

Figure S1. Wind trajectories retrieved from the MISR-MINX software tool (in units of knots) for the Williams Flats Fire. Half-barbs indicate 5 knots, full barbs are 10 knots. The grey lines represent the regional boundaries within the plume (See Fig. 1a). Empty circles are points where the retrieved wind speed was zero. Note: Only every tenth wind vector is plotted here to avoid over-crowding.
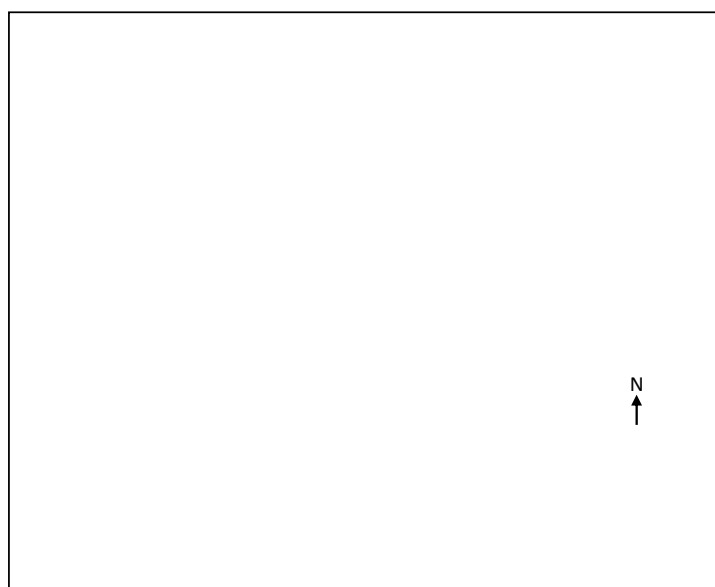

Figure S2. Percent relative humidity observed from the FIREX DC-8 aircraft for the Williams Flats Fire on 06 August 2019.
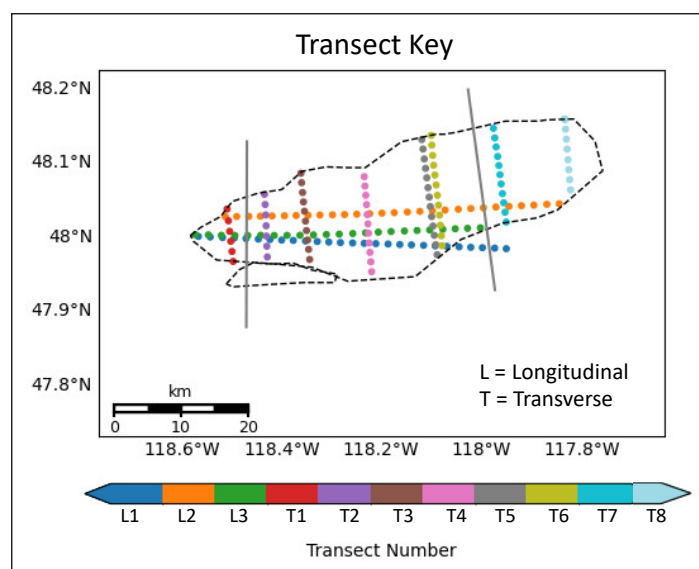
Figure S3. The location of sampling for the eight across-plume transects (T) and three along-plume transects (L).

Table S1. MISR components from Research Aerosol (RA) retrieval results, using the algorithm version summarized in Sect. 2.1, with a 774-mixture climatology. SSA—single scattering albedo.

Particle Size, Shape, Absorption	r_e (µm)[a]	SSA (446 nm)	SSA (558 nm)	SSA (672 nm)	SSA (866 nm)	Code [b]
Very small, spherical, strongly absorbing (flat)	0.06	0.84	0.79	0.73	0.62	VSmSphSab(f)
Very small, spherical, strongly absorbing (steep)	0.06	0.76	0.80	0.83	0.76	VSmSphSab(s)
Very small, spherical, moderately absorbing (flat)	0.06	0.92	0.89	0.86	0.78	VSmSphMab(f)
Very small, spherical, moderately absorbing (steep)	0.06	0.88	0.90	0.90	0.87	VSmSphMab(s)
Small, spherical, strongly absorbing (flat)	0.12	0.81	0.79	0.78	0.74	SmSphSab(f)
Small, spherical, strongly absorbing (steep)	0.12	0.72	0.80	0.87	0.84	SmSphSab(s)
Small, spherical, moderately absorbing (flat)	0.12	0.90	0.89	0.88	0.85	SmSphMab(f)
Small, spherical, moderately absorbing (steep)	0.12	0.85	0.90	0.93	0.92	SmSphMab(s)
Medium, spherical, strongly absorbing (flat)	0.26	0.78	0.80	0.80	0.81	MeSphSab(f)
Medium, spherical, strongly absorbing (steep)	0.26	0.70	0.80	0.88	0.89	MeSphSab(s)
Medium, spherical, moderately absorbing (flat)	0.26	0.89	0.90	0.90	0.90	MeSphMab(f)
Medium, spherical, moderately absorbing (steep)	0.26	0.83	0.90	0.94	0.94	MeSphMab(s)
Very small, spherical, non-absorbing	0.06	1.0	1.0	1.0	1.0	VSmSphNab
Small, spherical, non-absorbing	0.12	1.0	1.0	1.0	1.0	SmSphNab
Medium, spherical, non-absorbing	0.26	1.0	1.0	1.0	1.0	MeSphNab
Large, spherical, non-absorbing	1.28	1.0	1.0	1.0	1.0	LaSphNab
Large, non-spherical, weakly absorbing	1.21	0.91	0.95	0.97	0.98	LaNsphWab

[a] Each component has a designated effective radius (r_e).; [b] The code for each component includes four elements: size—very small (VSm), small (Sm), medium (Me), and large (La); shape—spherical (Sph) or non-spherical (Nsph); light absorption—non-absorbing (Nab), weakly absorbing (Wab), moderately absorbing (Mab), and strongly absorbing (Sab); spectral light absorption profile—equal in all spectral bands (flat), or varying between spectral bands (steep).

Supplementary Material, Part 2

We present in the second section of this supplement detailed descriptions of the *in situ* and spacecraft observations collected for the Williams Flats Fire, by transect. (This elaborates on Sections 3.1 and 3.2 in the main text.) We also provide a separate, detailed discussion of the DIAL-HSRL measurements for both along- and across-plume transects, including line-graphs of the relevant measurements as a function of downwind distance from the fire source.

I.   Satellite Observations of the Williams Flats Fire

The sections below use the regional statistical data from Table 1 in conjunction with the lat/lon plots in Figures 3-5 to characterize in detail each plume region, with emphasis on the *differences* from one to the next. This allows us to both quantify large-scale patterns as well as to visualize small-scale changes, and to account for any differences in sample size.

Region I
The near-source region, within ~33 min of the source, is strongly characterized by moderate-to-high REPA, with a mean SSA of ~0.87 and a low SD indicating little variability (Figure 3, Table 1). This can be attributed to: 1) very high mean and median fractions of the spectrally flat, BC-like component throughout the region (60% and 74% respective contributions to the mid-visible AOD); and 2) smaller AOD fractions of weakly-absorbing non-spherical aerosols (mean ~5%) and moderately absorbing, spectrally steep BrC-like aerosols (mean ~8%), both of which are significant contributors to total AOD along the northern plume edge. Regional REPS is overall small, with a mean extinction Ångström exponent (ANG) of ~1.57; however, there is some across-plume variability, with slightly larger aerosols retrieved in northern half of the region. Component analysis indicates REPS is the result of a mixture of mostly "small" aerosols, but with significant fractions of "very small" and "large" particles to the north, as per the MISR size categories defined in Table S1 (Figure 5).

Region II
The mid-plume region, with smoke aged ~33 to 140 min, displays significantly lower REPA (mean SSA ~0.94), characterized by a sharp decrease in the BC AOD fraction (mean ~25%), and a near-doubling of the non-absorbing aerosol fraction (mean ~50%). The northern regional edge exhibits significant contributions by both BrC- and dust-analog particles, leading to slightly increased regional mean fractions, although their contributions are negligible elsewhere within the region. REPS is also higher than in Region I, with mean ANG reduced to 1.3, but particles are still fine overall except in pixels that contain high fractions of the non-spherical and BrC components. This geographic variability is reflected in component analysis of the four size categories, with the northern edge of the region retrieved as a mixture of large and very small aerosols, whereas the rest of the region is dominated by medium and small particles (Figure 5). In general, the regional increase in REPS appears to be driven mostly by increased fractional contributions from medium particles (and to a lesser extent, large particles) accompanied by a decreased fractional contribution from small aerosols. Furthermore, these changes are also reflected in increased *absolute* AOD of the medium particles, and possibly also for the small size category.

Region III
The downwind region, where smoke is estimated to be between about 140 and 200 min from the source, displays a small reduction in REPA (mean SSA ~0.95), reflected in small decreases in each of the absorbing components accompanied by a large increase in the non-absorbing aerosol fraction (mean ~69%). Of the

remaining absorbing aerosols, BC is still by far the dominant contributor, with a mean fraction of over 20%. The absolute AOD of all four aerosol types appears to decrease (Figure 4), which suggests that new particle formation is not significant and if it occurs, is outweighed by aerosol removal processes. Regional REPS decreases significantly relative to Region II, with a mean ANG of ~1.52, so aerosols in this region are still larger than those in Region I. The smoke here is retrieved as a mixture of mostly medium-sized particles throughout the region, with lesser contributions from small and very small aerosols (the latter being mostly confined to the northern half of the region) (Figure 5). Compared to Region II, there is a significant loss of the large particle fraction and an increase in the small particle fraction, which we interpret as the driver behind the general decrease in effective particle size.

Region IV

The southern plume region exhibits REPS and REPA that are in-between those seen in Regions I and II of the northern plume, with mean SSA ~0.90 and mean ANG ~1.42. Particles are retrieved as a mixture of primarily BC-like particles throughout the length of the region, although the BC particle fraction decreases slightly with downwind distance. Unlike in the northern plume, there is little to no contribution from BrC except for a handful of pixels along the southern border, and there is a negligible non-spherical aerosol fraction. On average, non-absorbing aerosols comprise at least a third of the AOD fraction, although near the source their contribution is little to none. Particle size is retrieved as nearly exclusively a mixture of small and medium aerosols (Figure 5).

II. Aircraft *in situ* Observations of the Williams Flats Fire

The sections below use the transect statistical data from Table 2 and the regional data from Table 3 in conjunction with the lat/lon plots in Figures 7-8 and particle size distributions from Figure 9 to characterize in detail each plume region and transect, with emphasis on the *differences* from one to the next. This allows us to both quantify large-scale patterns as well as to visualize small-scale changes, and to account for any differences in sample size. Occasionally, we abbreviate transects using the letter T followed by the number of the transect (T1, T2, etc.) For the "remote sensing" longitudinal transects, we use the letter L (L1, L2, and L3). Taking the difference in observation timing into account, T1 is near the downwind end of MISR Region I in terms of smoke age, T2-T6 traverse MISR Region 2, and T7 and T8 fall within MISR Region 3 (Figure 1). L1 observed the plume within minutes of MISR, whereas L2 and L3 sampled the plume later (refer to Figure S3 for the locations of sampling for all transects). Where possible, we emphasize comparisons between transect-to-transect particle property differences and trends observed by MISR.

Transect 1

The first aircraft transect only sampled smoke emitted from the northwest source, with an estimated smoke age on the order of 30 minutes. The estimated MCE of 0.87 suggests burning is a mixture of flaming and smoldering. The mode particle size is firmly within the "very small" size category with peak D_P=0.148 μm; however, there is a broad distribution of aerosol size overall (Figure 9), and "small" aerosols comprise nearly 30% of the total aerosol fraction on average (Table 3, Figure 8b). The smoke sampled here is overall relatively fresh (-log[NO_x/NO_y] ~ 0.37) and moderately absorbing (SSA_{540} ~ 0.928). Note that the MISR-retrieved mid-visible SSA at the downwind end of Region I is ~0.92 or higher, comparable to the T1 values, and greater than the MISR values nearer the source (Figure 3d). Furthermore, MISR also suggests that the region is primarily a mixture of small and very small particles (Figure 5a-d).

Transect 2

The second transect sampled smoke with an estimated age of ~45 minutes, corresponding to the upwind part of MISR Region II terms of smoke age, although fresher smoke from the southeast hotspot begins to converge with the rest of the plume at this point and so actual smoke age may vary north to south. The influx of new smoke is reflected in a reduction in transect-averaged oxidation and no significant increase in SSA values (~0.323 and 0.927 respectively) compared to T1. There are sharp increases in both absolute and dilution-corrected BC, CCN, and total aerosol concentrations relative to T1 (Table 2), which are well outside the range of measurement uncertainties. The CO-normalized estimates of BrC-only and BC-only absorption also dramatically increase compared to T1, with a particularly strong increase in BC-only absorption. The increase in the normalized BC mass and absorption are likely due to differential BC emissions relative to CO between the northwest and southeast hotspots, with the southeast hotspot producing comparably more BC-like smoke particles that are injected into the main plume here. Particle size is also overall smaller and narrower in range at T2, with decreased mean and mode particle size as well as decreased $D_{(90\%)}$ (i.e., the size below which 90% of the particle are found) (Table 2). This is also likely due to the influx of fresher smoke, which tends to contain smaller particles. Estimated transect-averaged MCE is slightly higher (~0.89), indicating flaming conditions may have been somewhat more favored for smoke in this transect compared to T1. This would follow from the idea that there are higher BC emissions in this transect as flaming conditions tend to emit higher fractions of BC. Note that, similarly, MISR observes higher fractions of BC AOD and overall slightly smaller particle size in the southern plume compared to the northern plume (Figure 4b, 5). Furthermore, the MISR-observed mid-visible SSA in the southern plume is mostly ~0.92 or lower in the approximate sampling location of T2, which may explain why the merged northern and southern smoke in T2 does not exhibit strong changes in SSA despite the decreased REPA in the northern plume component (Figure 3d). Lastly, as the northern and southern components are distinct at the time of MISR observation, we do not observe an increased AOD for smoke of similar age, which one might expect from increased CO mixing ratios and aerosol concentrations measured *in situ*.

Transect 3

Estimates place smoke age in T3 at approximately one hour, about a quarter of the way into MISR Region II in terms of smoke age, and MCE is nearly identical to that in T2. Smoke from the southeast hotspot continues to be mixed into this sample as it was at T2; this can be seen in the increased CO mixing ratio in Figure 1c and further increases in absolute and normalized measurements of BC mass and CCN number concentrations, although the change in BC is just within the range of the SP2 uncertainty. These changes are accompanied by: increases in the mean and median aerosol size (D_P=0.141, $D_{(50\%)}$=0.155), increased oxidation state (~0.38), and a relatively static normalized total aerosol count compared to T2. The differences in trends from T2 to T3 compared to trends from T1 to T2 are important: between T1 and T2 we see that increased CO mixing ratio, BC mass, and CCN concentrations are correlated with *smaller* particles of *higher* number concentrations displaying *decreased* levels of aging (oxidation), whereas between T2 and T3 the CO, BC, and CCN trends are correlated with *larger* particles of roughly the *same* number concentration displaying *increased* levels of aging. This *may* suggest that the increase in BC and CCN concentrations reaching T3 is not as driven by the injection of fresher particles as it is by particle growth via coagulative processes, where previously ultrafine BC particles below the size detection limit of the SP2 and LAS (~0.09 μm) have aggregated to form larger aerosols or coalesced onto existing ones. This method of particle growth is known to be important in areas of dense smoke where aerosol concentrations are high, as is the case here, yet the smoke here is considerably downwind from both sources. However, this process would also account for the fact that the normalized aerosol count does not increase with the BC mass, as these particles would just be growing larger rather than more numerous. Additionally, larger and/or more

aged particles tend to be more efficient CCN, which would account for the increased CCN number concentration. However, particle growth here is also likely due to condensational growth. Contrary to expectations, the increased oxidation is not accompanied by an increase in SSA (actually a slight decrease to ~0.924, although, as with the SSA change in T2, this may be within the range of uncertainty of the PSAP/neph measurements). Lastly, this transect exhibits slight enhancements of both BC-only and BrC-only absorption of similar magnitude. Note that the increasing aerosol size in T3 corresponds with an increase in REPS from MISR for smoke of similar age in the northern plume. However, as mentioned in the discussion of T2, the MISR plume does not exhibit increased AOD for smoke of similar age since the northern and southern components had not yet merged at the time of MISR observation.

Transect 4
Burning conditions for smoke observed in T4 are firmly in the flaming category, with MCE ~0.93 (the highest of all transects), and the smoke is estimated at about 85 minutes old at the time of observation, about the middle of MISR Region II in terms of smoke age. The smoke is significantly more oxidized here compared to T3, with $-\log[NO_x/NO_y]$ ~0.55, although again the change in SSA is very small (an increase to 0.928, within the range of instrument uncertainty). Both BC- and BrC-only absorption decrease, as do the absolute and normalized measurements of CCN, BC, and total aerosol count, the latter of which is within the range of uncertainty (for the normalized measurement) and so might not be a reliable indicator of true particle dilution or loss. The particle size distribution is essentially identical to that in T3 despite the reduced number concentration, suggesting that if there is particle loss between these transects then it is not size-selective.

Transect 5
The transect-averaged MCE at T5 slightly decreases to ~0.88 and smoke is estimated at 112 minutes old, roughly three-quarters of the way downwind within MISR Region II in terms of smoke age. Despite a decrease in the mode aerosol size (Peak D_P=0.134 μm), at least some particles increase in diameter, as seen by an increased $D_{(90\%)}$; this is accompanied by decreases in the CO-normalized aerosol count and the absolute and normalized CCN number and BC mass concentrations; however, all these differences are within the instruments' uncertainty ranges. Oxidation continues to increase with $-\log[NO_x/NO_y]$ ~0.63, which is accompanied by decreased mid-visible absorption (SSA~0.934) and decreases in BrC and BC absorption specifically. Note that MISR observes a relatively significant fractional increase in large aerosols for smoke of similar age along the northern edge here, with a corresponding decrease in ANG. The total MISR AOD also decreases in this same area.

Transect 6
The average MCE in T6 is ~0.89, and smoke age is estimated at 115 minutes old, essentially the same as T5, so differences might better indicate internal plume variability or measurement uncertainty rather than trends in particle evolution. Particle size in T6 is overall slightly larger (Peak D_P=0.155 μm vs. 0.134 μm for T5) and with a narrower distribution width compared to T5. Oxidation values differ only slightly (~0.647 compared to ~0.63 for T5). There is a large decrease in both the absolute and normalized BC mass concentration (951 vs. 1120 ng/m^3 and 2.88 vs. 3.33 ng/ppm*m^3, respectively), despite a small decrease in SSA (~0.929). The SSA change is likely driven by an increase in BrC-only absorption, which increases for the first time since T3. Particles are also more hygroscopic in T6, with both absolute and normalized CCN concentrations increasing (6567 vs. 5377 #/cc and 19.89 vs. 15.78 #/cc*ppb, respectively). The differences between T5 and T6 illustrate the extent to which measured particle properties can differ for smoke of nearly the same age, placing in context the observed differences between MISR and the DC-8.

Transect 7

Smoke in T7 is approximately 140 minutes old, emitted with an estimated MCE of 0.89, near the boundary between MISR Regions II and III. Particle oxidation values increase to ~0.734, reflecting a significant change in the degree of aerosol aging at this point. Particle size is slightly larger than what was observed in T6 with increased $D_{(90\%)}$ and $D_{(10\%)}$; however, the normalized total aerosol count is essentially unchanged from that in T6. There is a decrease in both absolute and normalized concentrations of BC mass and CCN number, the former of which is mirrored in decreased BrC and BC absorption (leading to an increased SSA of 0.936, the largest single transect-to-transect change). These changes correspond with a similar area of transition for smoke of the same age as seen by MISR, where BC AOD decreases and SSA increases along the boundary of Regions II and III (Figures 3-4). Interestingly, there is an increase in the absolute total aerosol count compared to T6, which is most likely due to different sampling, as AOD is apparently not uniformly distributed in this area of the plume according to MISR (Figure 3b). Furthermore, smoke in this area approximately corresponds with the points at which MISR observes a decrease in particle size, reflected by a loss of large-size particles. This diverges from the *in situ* observations, but as explained the main text is likely due to differences in vertical sampling and gravitational settling of larger particles.

Transect 8

Estimates of smoke age are unavailable for T8 from the aircraft, but it is toward the downwind end of MISR Region III, perhaps close to 200 min from the source. Interestingly, oxidation values indicate the smoke is not as well oxidized as in T7 (~0.687, vs. ~0.734 for T7). Particles are also less hygroscopic and less absorbing (SSA ~0.94), and there is a large increase in particle size, reflected in increased $D_{(50\%)}$ and $D_{(90\%)}$. Furthermore, the width of the distribution is comparatively larger than in T7. This could reflect the influence of background aerosols, as MISR retrievals suggest the background particle size distribution is influenced by all four size categories to some degree, while smoke of similar age to T8 is mainly influenced by medium and small aerosols.

DIAL_HSRL Measurements

Large values of the DIAL-HSRL depolarization ratio are typically driven by ice or dust particles (30-40%) and differ significantly from the less depolarizing particles such as urban pollution or smoke. With few exceptions, the aerosol depolarization ratios (vertical median values) at both 532 and 1064 nm are consistently between 3-6% within the Williams Flats plume (Figures S4-S7), typical of fresh biomass burning smoke (Burton et al., 2013]). There are only small changes in depolarization at both wavelengths along the length of the plume and these are within the variability of the measurement. Furthermore, there is little vertical variation in the depolarization ratios across the plume, suggesting that any non-spherical component is not stratified within the smoke layer. Within the plume, the less polarizing smoke particles dominate the depolarization values. However, the larger depolarization values seen just outside and above the smoke plume (Figure 6 in the main text) suggest that background dust is present in the air layer, which is seen by MISR along the plume's northern edge.

The 1064/532 nm color ratio is typically between 0.5-0.7 inside the plume, with a notable exception in L3, where values as high as 0.9 were observed near the boundary of MISR Regions I and II (Figures S8-S11). Otherwise, only small, unsystematic changes (typically <<0.1) are seen along the length of the plume and between times of observation, which are well within the measurement variability. Burton et al. (2013) indicate ranges of color ratio from fresh smoke to be 0.40-0.48 (note: author uses color ratio as 532/1064 nm). Larger color ratios can indicate larger aerosols; however, there is no clear numerical separation between

large and small particles. Although data from the LAS suggest particles increasing in size as the plume evolved, these changes are small enough that they are not reflected in the color ratio observations.

The lidar ratio, for the most part, ranges from ~35-45 sr^{-1} throughout the plume, although there are several points where its value exceeds or dips below this range. The values are in line with those previously observed for fresh smoke (Burton et al., 2012, 2013). In all three longitudinal overpasses as well as the across-plume transects, the lidar ratio systemically increases with downwind distance from the source within the first few hours (Figures S8-S11). Existing literature also shows lower lidar ratios for fresh smoke than aged smoke (e.g, Burton et al., 2012); however "aged" smoke in these studies is sampled at time scales much longer than those observed in the Williams Flats Fire (on the order of 1-2 days rather than several hours old). The reason for the increase in lidar ratio with age requires further investigation, especially over these shorter time scales. In this case, it is generally correlated with decreasing absorption, increased particle size, increased oxidation, and variable hygroscopicity observed in Table 2. (Note that although the transect-by-transect changes in these properties are often small, they are systematic and significant when taken across the whole plume.) One of these particle property changes might also be acting to decrease the backscatter relative to the extinction (which is the sum of absorption and scattering); this topic requires further study.

References:

Burton, S. P.; Ferrare, R. A.; Hostetler, C. A.; Hair, J. W.; Rogers, R. R.; Obland, M. D.; Butler, C. F.; Cook, A. L.; Harper, D. B.; Froyd, K. D. Aerosol classification using airborne High Spectral Resolution Lidar measurements – methodology and examples. *Atmos. Meas. Tech.* **2012**, *5*, 73–98, doi:10.5194/amt-5-73-2012.

Burton, S. P.; Ferrare, R. A.; Vaughan, M. A.; Omar, A. H.; Rogers, R. R.; Hostetler, C. A;, Hair, J. W. Aerosol classification from airborne HSRL and comparisons with CALIPSO vertical feature mask. *Atmos. Meas. Tech.*, **2013**, *6*, 1397 1412, doi:10.5194/amt-6-1397-2013.
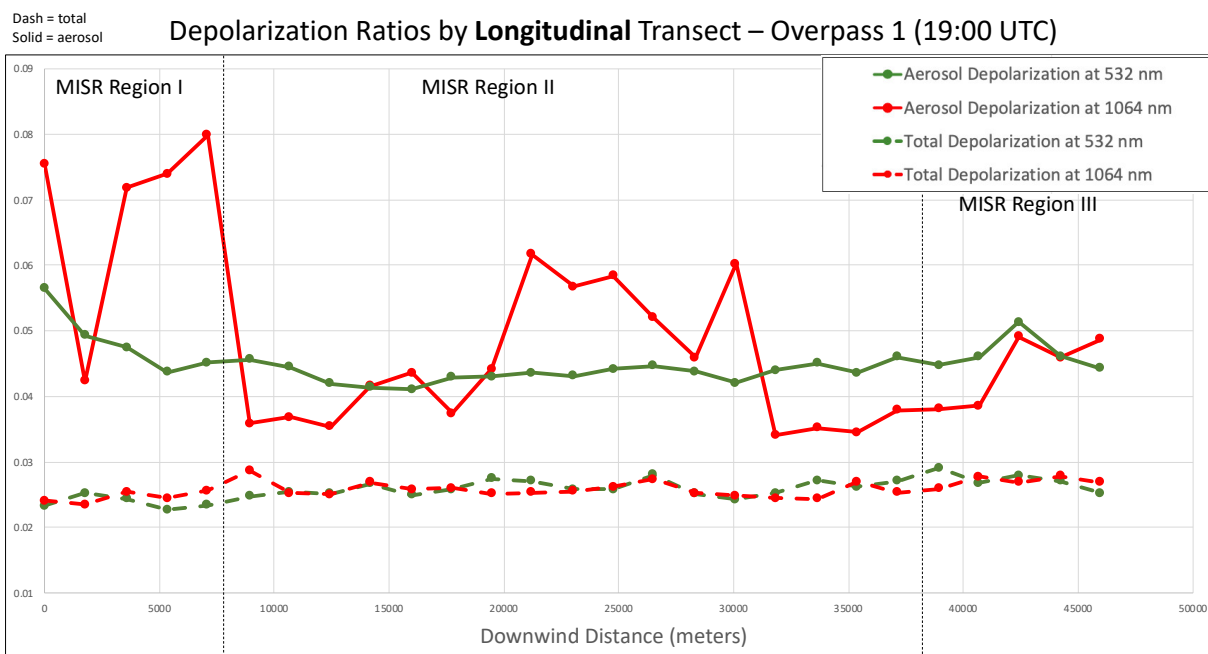
Figure S4. Median total volume and aerosol depolarization values retrieved by the DIAL-HSRL instrument during the first longitudinal overpass at ~19:00 UTC (L1). Indications of the dividing lines between the MISR Regions I-III are provided as dotted lines.
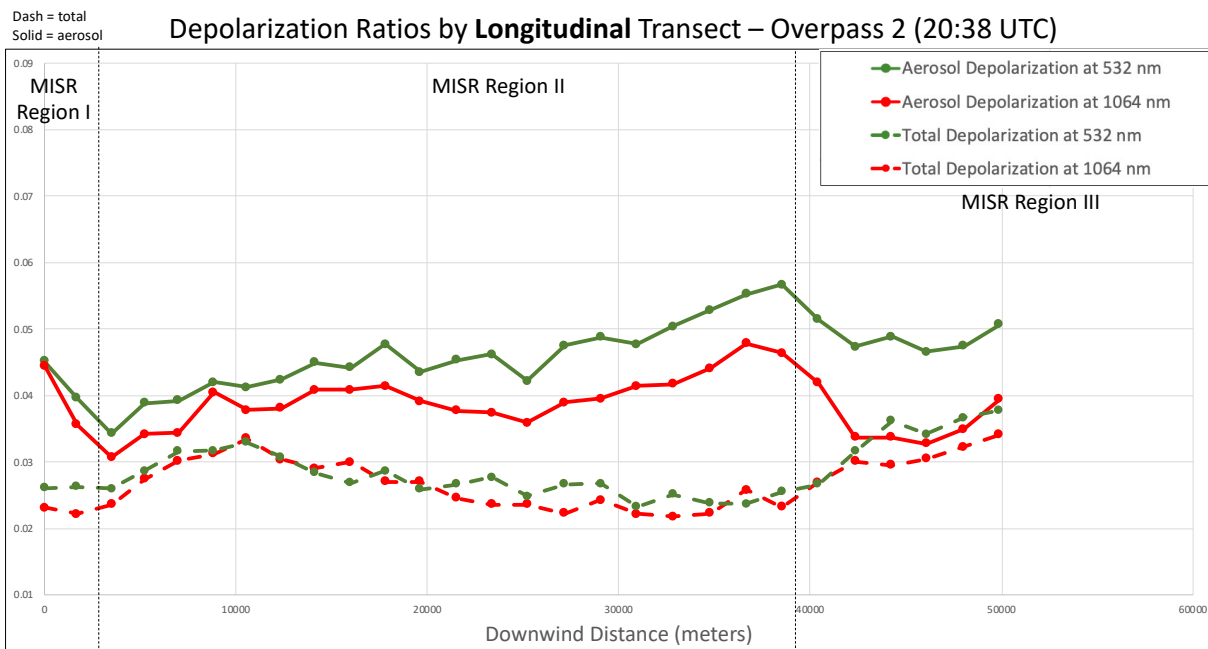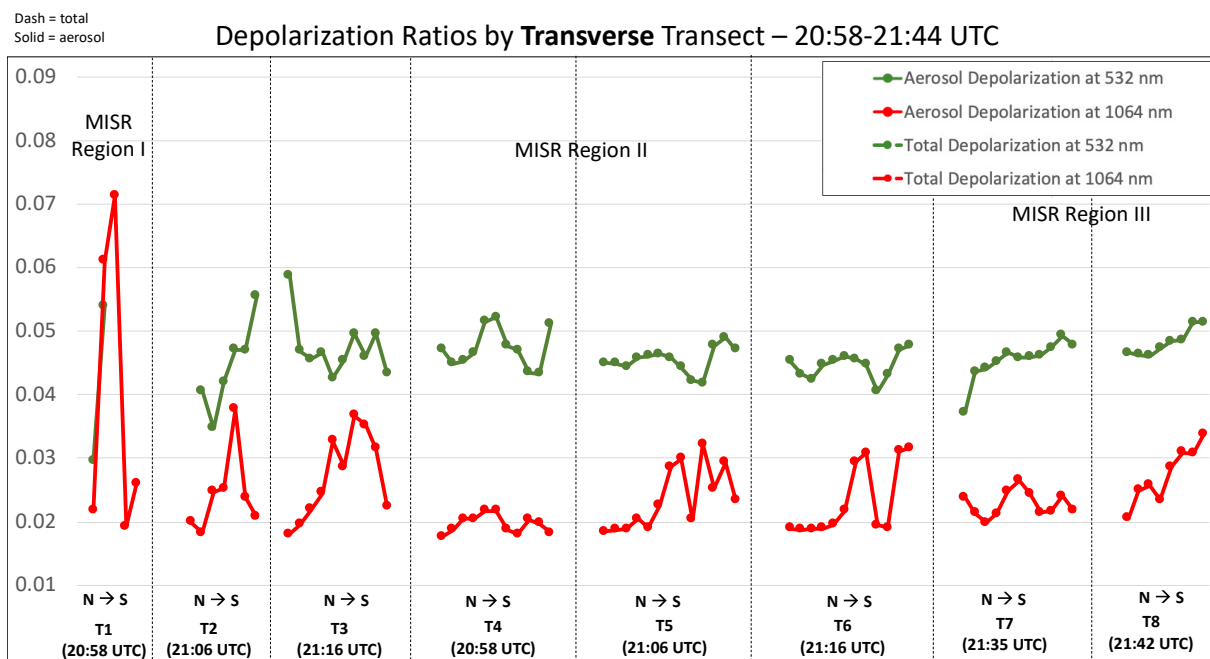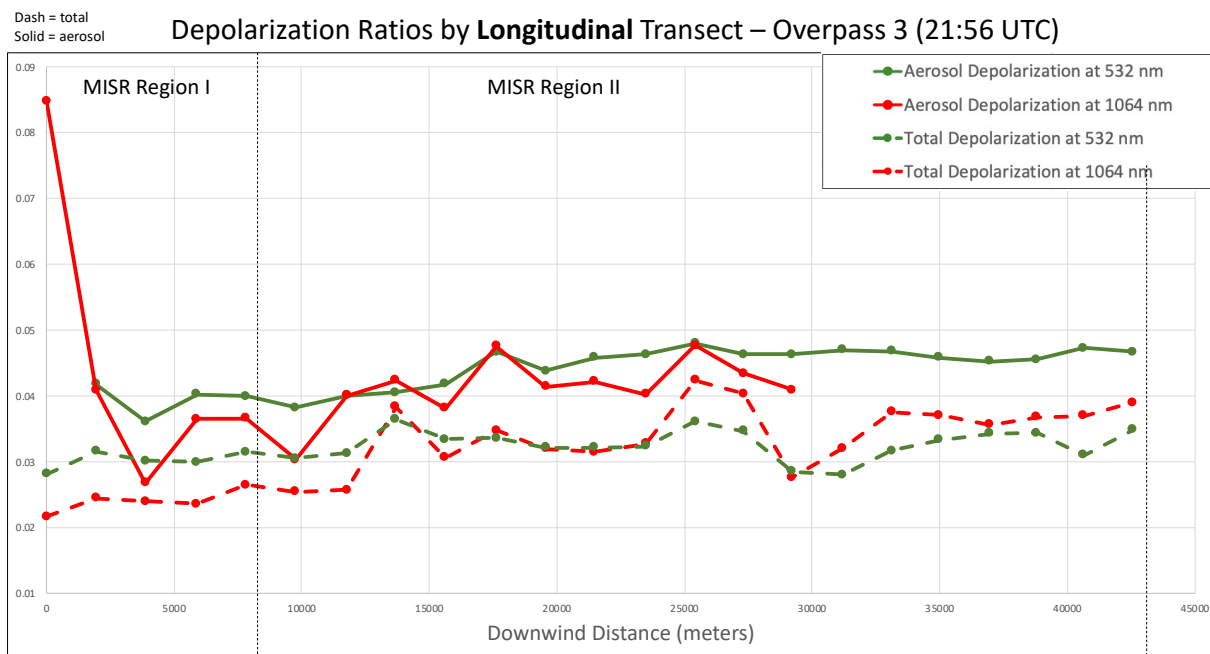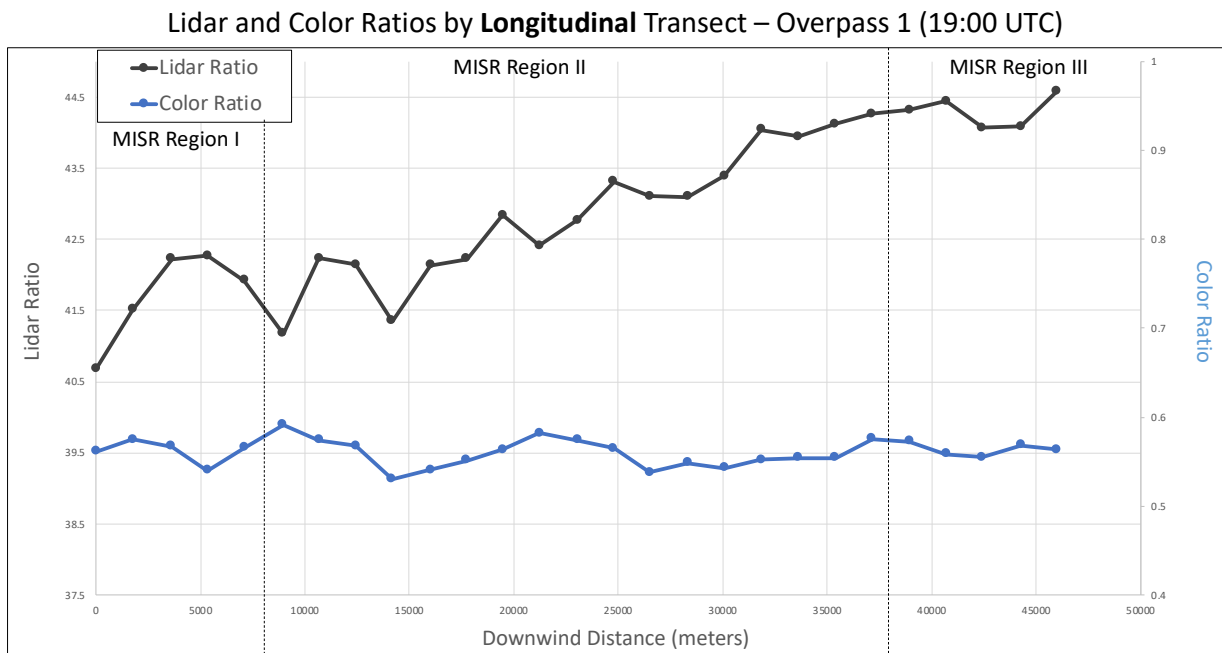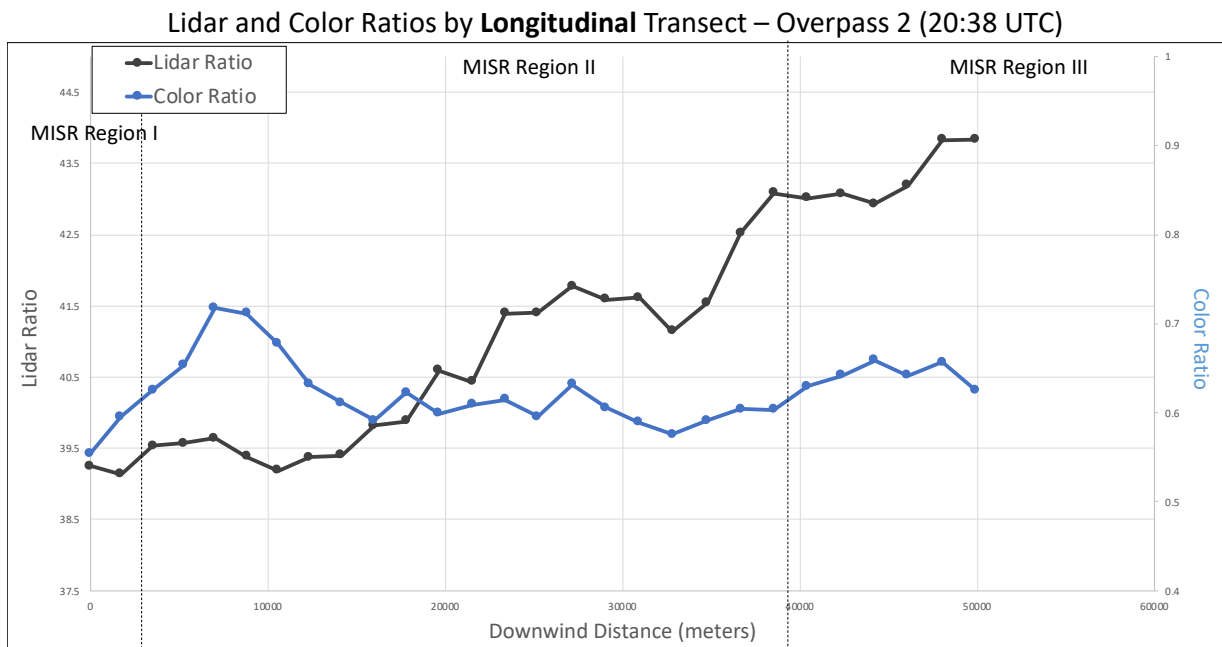

Figure S5. Median total volume and aerosol depolarization values retrieved by the DIAL-HSRL instrument during the second longitudinal overpass at ~20:38 UTC (L2). Indications of the dividing lines between the MISR Regions I-III are provided as dotted lines.

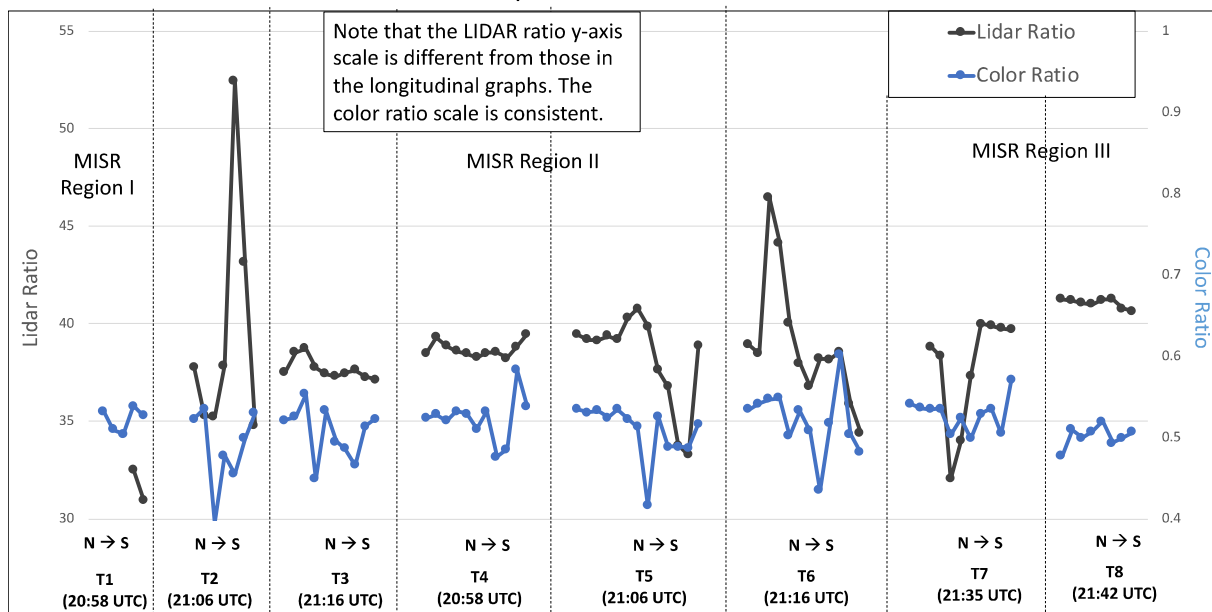**Figure S6.** Median total volume and aerosol depolarization values retrieved by the DIAL-HSRL instrument during the eight along-plume transects (T1-T8). The dotted lines separate the transects from one another, the data from which are ordered north to south. Approximate locations of the MISR Regions I-III are labeled.

Figure S7. Median total volume and aerosol depolarization values retrieved by the DIAL-HSRL instrument during the third longitudinal overpass at ~21:56 UTC (L3). Indications of the dividing lines between the MISR Regions I-III are provided as dotted lines.
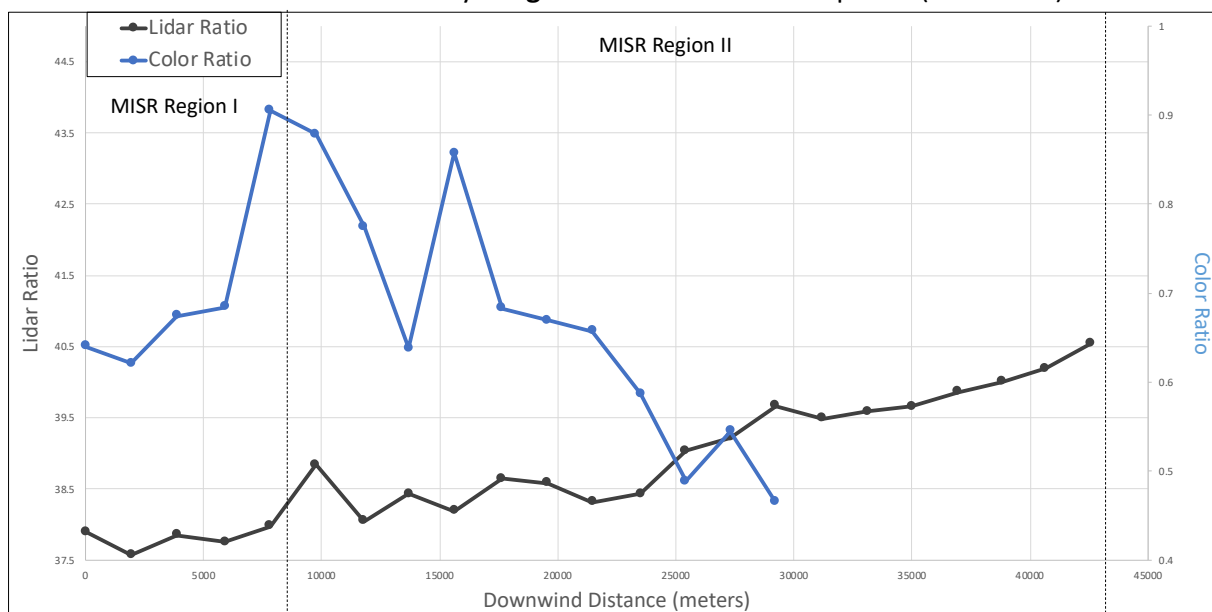
Figure S8. The lidar ratio and color ratio values retrieved by the DIAL-HSRL instrument during the first longitudinal overpass at ~19:00 UTC (L1). Indications of the dividing lines between the MISR Regions I-III are provided as dotted lines.

Figure S9. The lidar ratio and color ratio values retrieved by the DIAL-HSRL instrument during the second longitudinal overpass at ~20:38 UTC (L2). Indications of the dividing lines between the MISR Regions I-III are provided as dotted lines.

Lidar and Color Ratios by **Transverse** Transect – 20:58-21:44 UTC

Figure S10. The lidar ratio and color ratio values retrieved by the DIAL-HSRL instrument during the eight along-plume transects (T1-T8). The dotted lines separate the transects from one another, the data from which are ordered north to south. Approximate locations of the MISR Regions I-III are labeled.

Lidar and Color Ratios by **Longitudinal** Transect – Overpass 3 (21:56 UTC)

Figure S11. The lidar ratio and color ratio values retrieved by the DIAL-HSRL instrument during the third longitudinal overpass at ~21:56 UTC (L3). Indications of the dividing lines between the MISR Regions I-III are provided as dotted lines.

Figures S12-S19 illustrate the standard deviation of the depolarization, color ratios, and lidar ratios displayed in Figures S4-S11. We show this variability separately so as to avoid crowding on individual graphs.
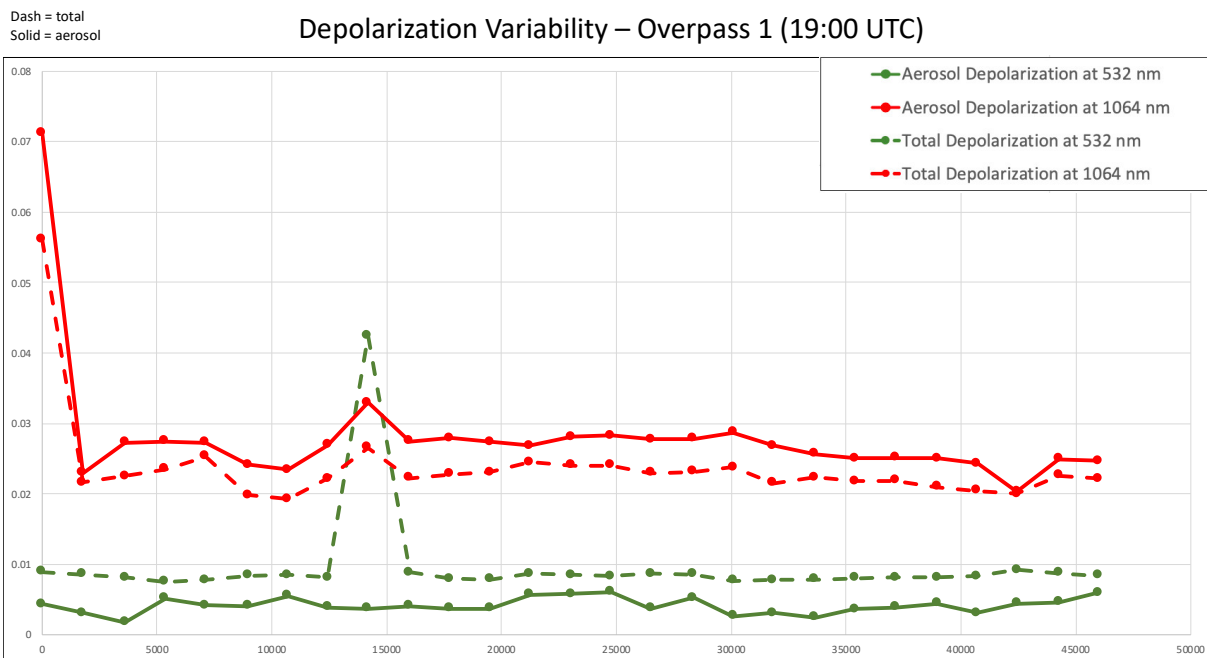
Figure S12. Standard deviation in the total volume and aerosol depolarization values retrieved by the DIAL-HSRL instrument during the first longitudinal overpass at ~19:00 UTC (L1) – Corresponds with S4.
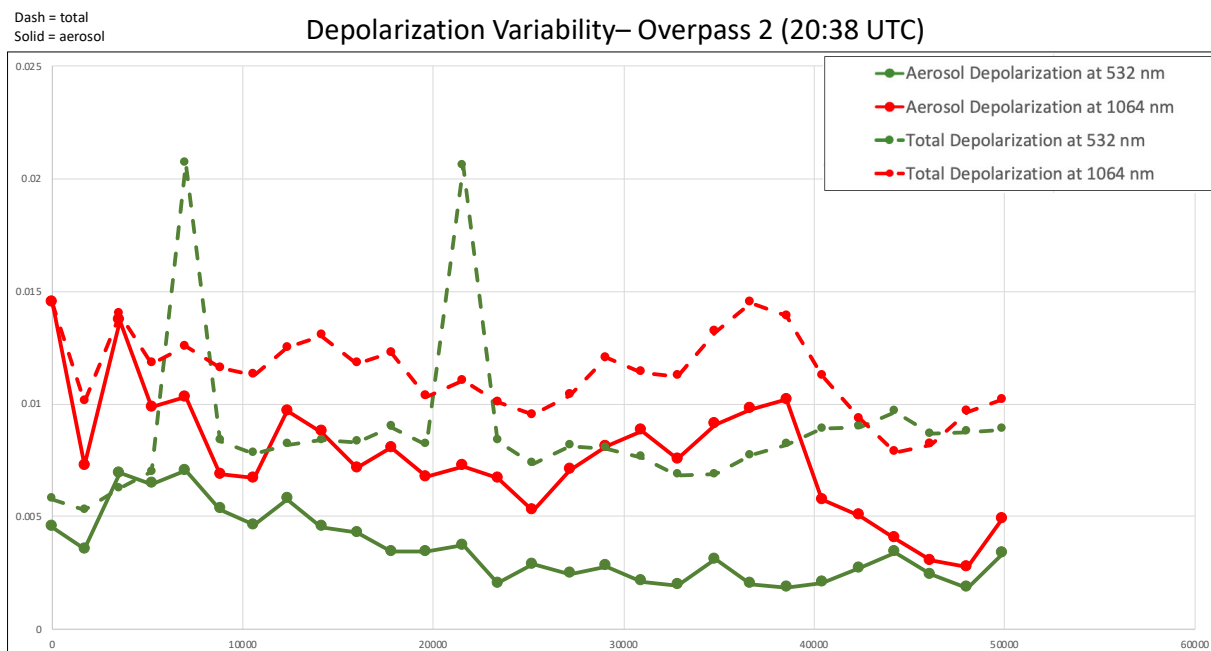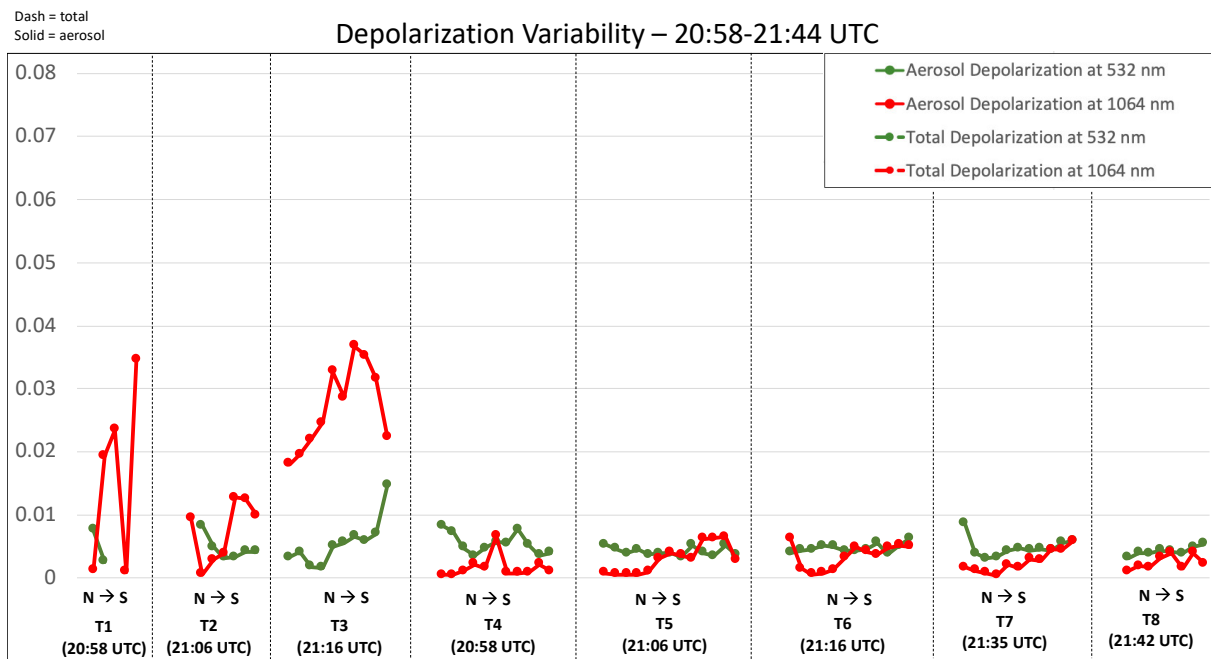

Figure S13. Standard deviation for the total volume and aerosol depolarization values retrieved by the DIAL-HSRL instrument during the second longitudinal overpass at ~20:38 UTC (L2). – Corresponds with S5.

Figure S14. Standard deviation for the total volume and aerosol depolarization values retrieved by the DIAL-HSRL instrument during the eight along-plume transects (T1-T8). The dotted lines separate the transects from one another, the data from which are ordered north to south -- Corresponds with S6.
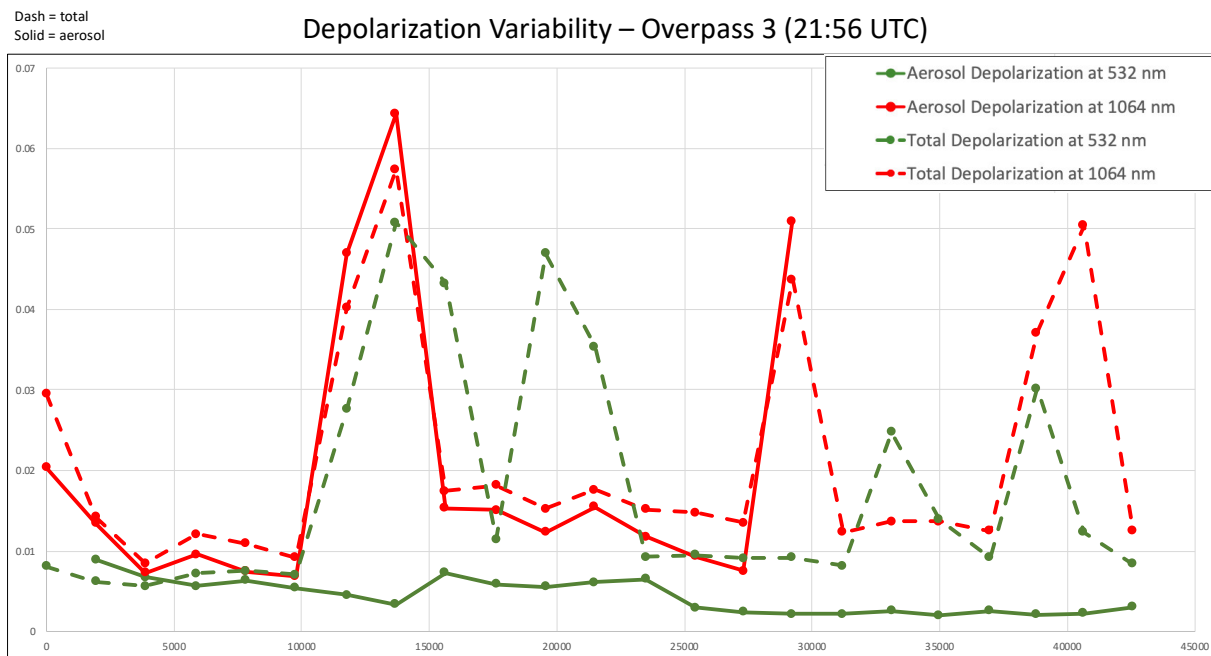

Figure S15. Standard deviation for the total volume and aerosol depolarization values retrieved by the DIAL-HSRL instrument during the third longitudinal overpass at ~21:56 UTC (L3) – Corresponds with S7.

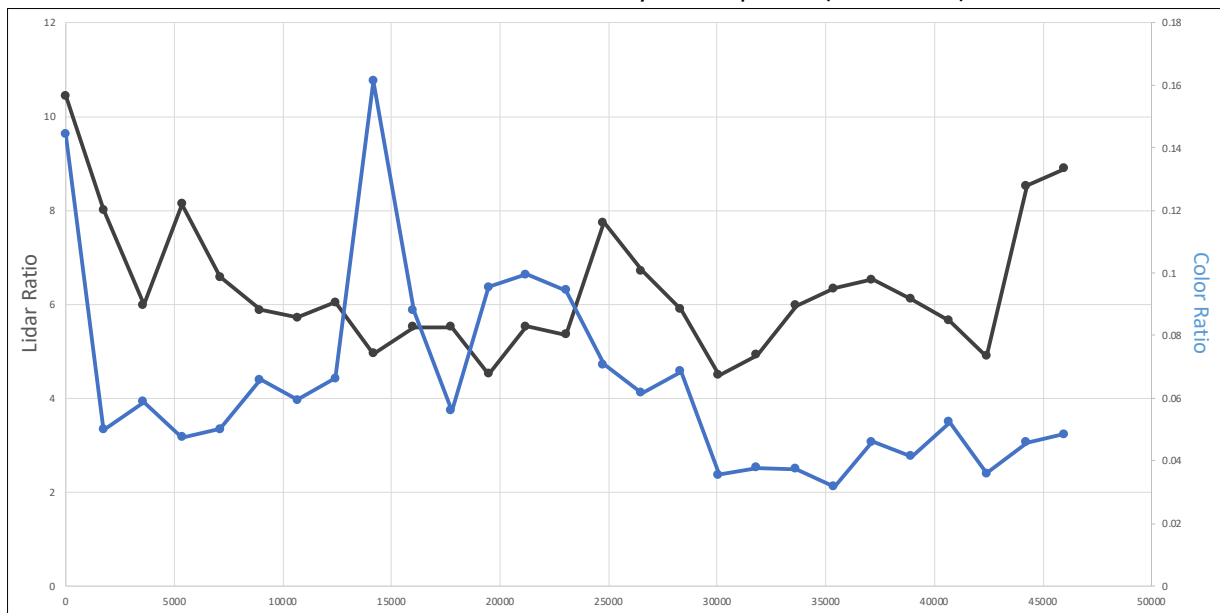## Lidar and Color Ratio Variability – Overpass 1 (19:00 UTC)

Figure S16. Standard deviation for the lidar ratio and color ratio values retrieved by the DIAL-HSRL instrument during the first longitudinal overpass at ~19:00 UTC (L1) – Corresponds with S8
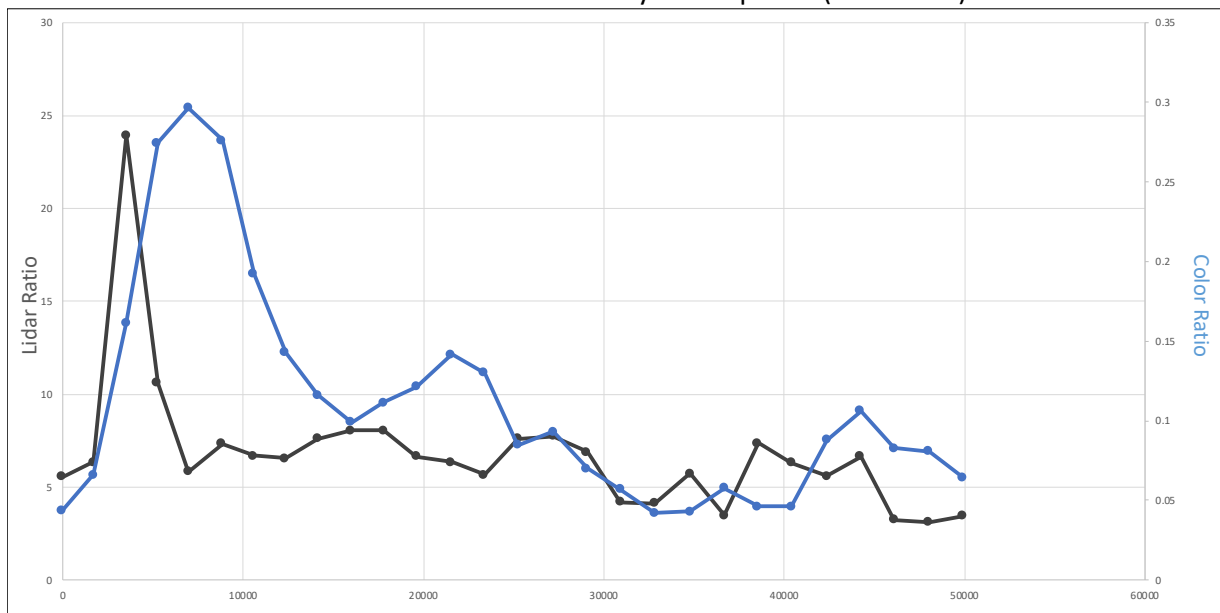
Lidar and Color Ratio Variability – Overpass 2 (20:38 UTC)

Figure S17. Standard deviation for the lidar ratio and color ratio values retrieved by the DIAL-HSRL instrument during the second longitudinal overpass at ~20:38 UTC (L2) – Corresponds with S9.
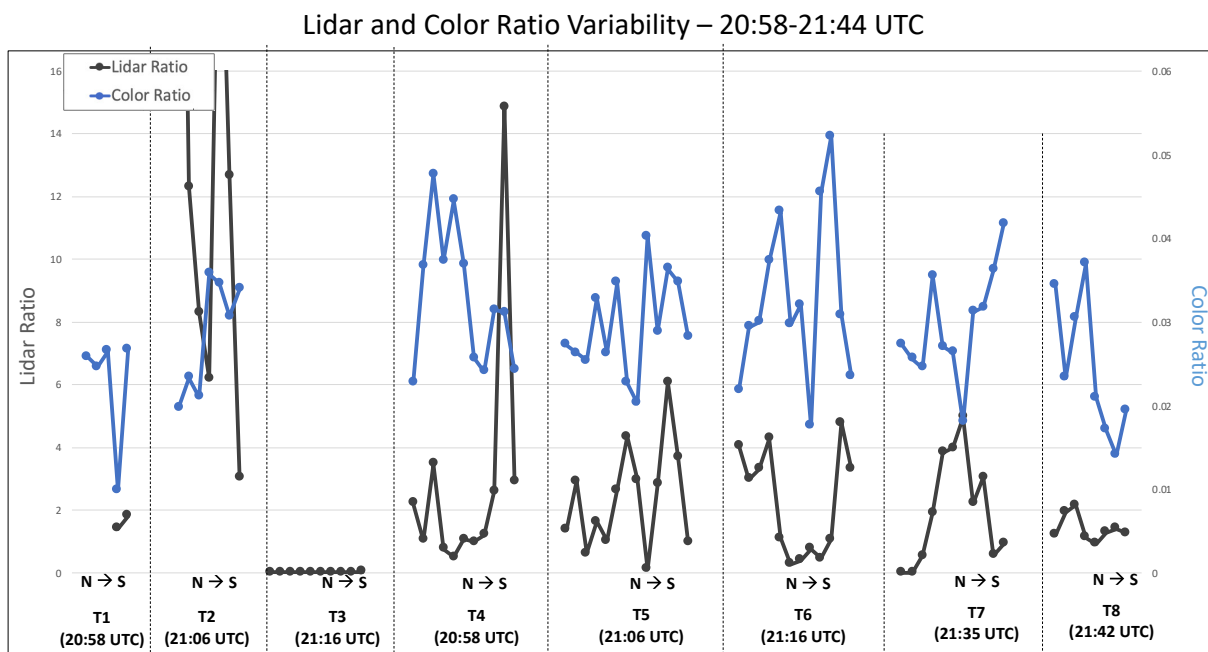
Lidar and Color Ratio Variability – 20:58-21:44 UTC

Figure S18. Standard deviation for the lidar ratio and color ratio values retrieved by the DIAL-HSRL instrument during the eight along-plume transects (T1-T8). The dotted lines separate the transects from one another, the data from which are ordered north to south – Corresponds with S10.
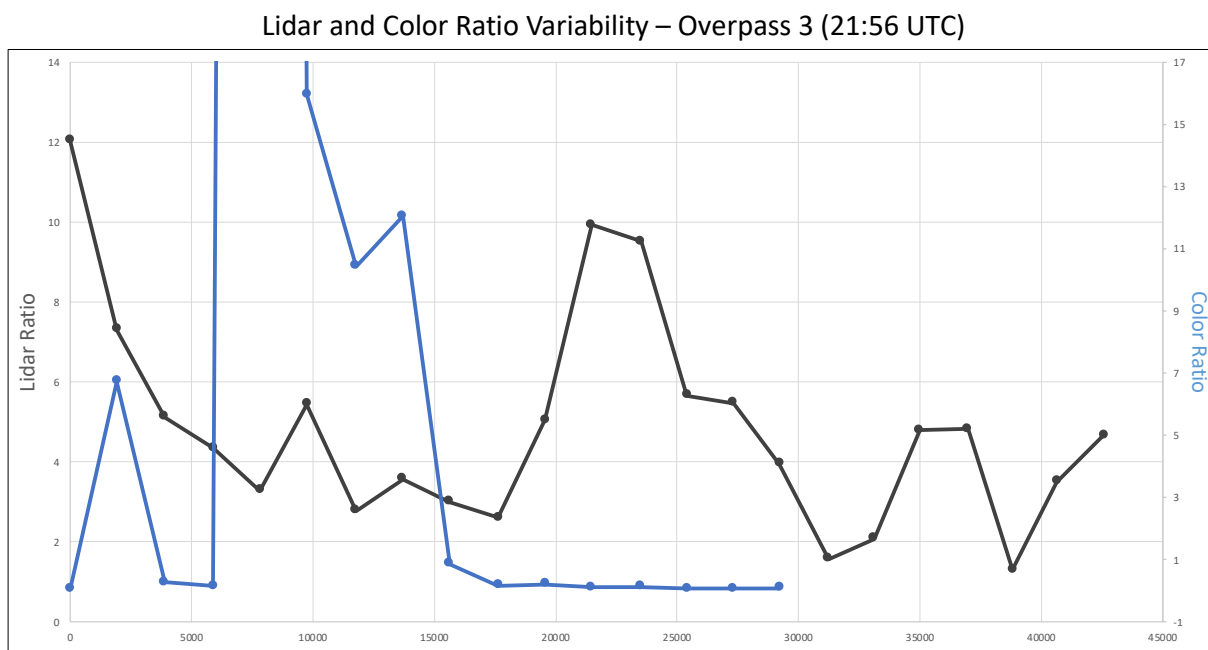
Lidar and Color Ratio Variability – Overpass 3 (21:56 UTC)

Figure S19. The lidar ratio and color ratio values retrieved by the DIAL-HSRL instrument during the third longitudinal overpass at ~21:56 UTC (L3) – Corresponds with S11.